Introducing a nested phase change agent with an acoustic response that depends on electric field: A candidate for myocardial perfusion imaging and drug delivery

Article · March 2018

DOI: 10.1016/j.apacoust.2018.03.028

CITATIONS
0

READS
55

7 authors, including:

Michael Jeffrey Cimorelli
Drexel University
10 PUBLICATIONS **0** CITATIONS
SEE PROFILE

Brett Angel
Drexel University
9 PUBLICATIONS **0** CITATIONS
SEE PROFILE

Benjamin Michael Andrien
Drexel University
2 PUBLICATIONS **0** CITATIONS
SEE PROFILE

Kyle Barrett
Drexel University
6 PUBLICATIONS **10** CITATIONS
SEE PROFILE

Applied Acoustics 138 (2018) 9–17

Contents lists available at ScienceDirect

Applied Acoustics

journal homepage: www.elsevier.com/locate/apacoust

Introducing a nested phase change agent with an acoustic response that depends on electric field: A candidate for myocardial perfusion imaging and drug delivery

Michael Cimorelli[a], Brett Angel[b], Aaron Fafarman[a], Andrew Kohut[b], Benjamin Andrien[a], Kyle Barrett[a], Steven Wrenn[a,*]

[a] Chemical and Biological Engineering, Drexel University, Philadelphia, PA, United States
[b] Cardiology, Drexel University College of Medicine, Philadelphia, PA, United States

ARTICLE INFO

Keywords:
Nested droplets
Phase change
Voltage-activated
Ultrasound contrast
Perfluorocarbon
Myocardial perfusion

ABSTRACT

We present a voltage-sensitive phase change agent comprising an aqueous emulsion of surfactant-coated liquid perfluorocarbon droplets nested within a negatively charged phospholipid bilayer. The sensitivity to voltage allows, via exposure to an electric field, acoustic activation of the perfluorocarbon droplets at an ultrasound intensity that is otherwise insufficient to cause activation. The result is a phase change agent for which activation depends not on ultrasound intensity but rather on the presence of an electric field. Accordingly, we offer the first enhanced ultrasound contrast agent ("Electrast") that takes advantage of the electrical activity of the heart and leads to selective activation at a fixed mechanical index (MI). Being voltage-sensitive, Electrast activates selectively in the coronary circulation, giving enhanced ultrasound contrast within the myocardium while leaving other regions largely unenhanced. Specifically, in a closed chest swine study, the contrast enhancement between the myocardium and the left ventricle increased by 36.4 dB ± 0.2 upon injection of a charged, nested PCA formulation at a fixed MI of 0.9 (GE Vivid *i*). Similar enhancement was observed in rats, and the contrast-to-tissue ratio increased by nearly 10 dB at an MI of 0.28 upon exposure to an electric field of 1 V/cm in a tissue-mimicking phantom. Additionally, ultrasound-induced leakage of calcein, a water-soluble fluorescent dye, from a nested, charged PCA formulation more than doubled at a peak negative pressure of 0.5 MPa upon exposure to an electric field of 0.25 V/cm. These results suggest that Electrast, a voltage-sensitive phase change agent, is a candidate for myocardial perfusion imaging using ultrasound.

1. Introduction

1.1. Brief history of nesting

We introduced nearly a decade ago a novel microbubble architecture that comprises coated microbubbles nested within the aqueous core of a microcapsule [1]. In subsequent years we described how a nesting shell enables ultrasound imaging that is longer-lasting [2–5] and safer [5,6] than imaging with conventional (that is, un-nested) microbubbles. The monolayer coating of a microbubble slows – by decreasing interfacial tension so as to lower the Laplace overpressure [7,8] and by increasing resistance to diffusion [9] – but does not prevent gas dissolution [9]; as a result, microbubbles do not survive exposure to a mechanical index (MI) > 0.3 [10,11]. When nested inside the aqueous core of a microcapsule, however, a microbubble dissolves only partially. This is because the nesting shell separates the aqueous core from the bulk, and the aqueous interior of the microcapsule becomes sufficiently concentrated with the gas it receives from the microbubble that mass transport ceases; the microbubble, though it shrinks somewhat, persists [3,4]. At MI values sufficiently low that an un-nested microbubble sustains oscillations, the monolayer coating of the microbubble influences the oscillations via dilatational viscosity, which impacts damping, and via area expansion modulus (Gibbs elasticity), which impacts the natural frequency [12]. The presence of a nesting shell further influences microbubble oscillations, allowing greater tuning of microbubble acoustic and cavitation phenomena than is possible with a monolayer coating alone [13,14]. In particular, a nested microbubble requires a higher ultrasound intensity (that is, a greater peak negative pressure) for inertial cavitation than does an un-nested microbubble [13]. In the context of imaging, the nesting shell improves safety both by increasing the inertial cavitation threshold pressure and by absorbing the energy of the shock wave generated by inertial cavitation – thereby protecting nearby cells – if

* Corresponding author.
E-mail address: spw22@drexel.edu (S. Wrenn).

https://doi.org/10.1016/j.apacoust.2018.03.028
Received 1 December 2017; Received in revised form 16 February 2018; Accepted 22 March 2018

inertial cavitation were to occur [6]. Employing a liposomal bilayer as the nesting shell allows theranostic applications of microbubbles beyond imaging, including ultrasound-triggered release as might find use in controlled drug delivery [15,16]. Furthermore, a bilayer nesting shell offers the possibility of fine-tuning the rate of release by tailoring shell composition; for example, one can combine cholesterol and phospholipids in a manner that sets the number and sizes of membrane domains (or lack thereof) [17–19], which in turn prescribes the kinetics and mechanism of release [1,20,21].

Herein we present a new nesting construct with a novel feature, namely voltage activation.

1.2. Voltage activation

In place of microbubbles, the new construct nests an emulsion of phase-change agents (PCAs), which are (typically perfluorocarbon) liquid droplets that have the potential to become gaseous microbubbles (that is, to change phase) once inside the body [22–25]. In the absence of a nesting shell, an advantage of PCAs over microbubbles is smaller size; whereas microbubbles have diameters in the micron range and are therefore limited to the intravascular space, PCAs can be prepared with diameters of nominally hundreds of nanometers such that they have the possibility to access the extravascular space [26]. This advantage of smaller size does not come free; the PCAs require vaporization after delivery into the body if they are to behave acoustically as microbubbles. Indeed, this was a motivation for developing condensation methods to produce PCAs that are easier to vaporize [27]by taking advantage of the fact that the energy required for vaporization depends on the perfluorocarbon species and droplet size [28].

In our view, the necessity to vaporize PCAs offers an opportunity for a new class of contrast agent.

Consider the following three facts: (1) a PCA of a given composition, droplet size, and interfacial coating has a fixed energy for vaporization; (2) vaporization generates a gaseous bubble that is larger than the initial liquid droplet; and (3) water is largely incompressible.

Taken together, the first two facts above mean that vaporization of a PCA liquid droplet requires both an energy input and room for expansion. Now imagine a PCA liquid droplet nested inside the aqueous core of a vesicle or microcapsule. The third fact then means that the PCA droplet cannot vaporize unless the nesting shell responds to provide the necessary room for expansion. In other words, the nesting shell poses an added resistance to vaporization. On one hand, this added resistance could be overcome with ultrasound alone simply by using a higher MI (than is needed to vaporize an un-nested PCA). On the other hand, one could design a nested PCA that works with both ultrasound and a second modality to activate PCAs in a selective manner; ultrasound of a given intensity would be sufficient to activate only those liquid droplets in nests acted on by the second modality, which interacts with the nesting shell to allow for acoustic activity.

This article describes the use of an electric field as the second modality to interact with charged nesting shells. Fig. 1 illustrates the concept. We demonstrate that a given formulation can be relatively dark (strictly speaking, silent) or relatively bright (noisy) at a given MI, the difference being due to the absence or presence of an electric field, respectively. We call this phenomenon, which occurs with electric field strengths that are orders of magnitude weaker and at least an order of magnitude slower (in the case of alternating current) than those associated with electroporation, “voltage activation.”

Applications involving voltage activation can proceed anywhere there is an electric field (e.g., endogenous or applied), need not induce a phase change to be visible with ultrasound, and need not be limited to ultrasound theranostics. In fact, one can think of voltage activation applications that do not use ultrasound; in the case of nested PCAs, a modality other than ultrasound could supply the energy for the phase change, and PCAs are not the only entities that could be nested inside a voltage-activated nesting shell. Still, the potential of using a voltage-activated ultrasound contrast agent for myocardial perfusion imaging - where the heart supplies the electric field - did not escape our notice.

1.3. Myocardial perfusion imaging

The idea of using ultrasound contrast agents for myocardial perfusion imaging is not new. Indeed, some echocardiographers with specialized skills are able to employ commercial microbubbles in an off-label manner, taking advantage of the aforementioned fact that microbubbles do not survive MI > 0.3 [11,29,30], some investigators have used PCAs directly [31], and others have used tethered PCAs and microbubbles, a construct they refer to as acoustic cluster therapy [32]. Additionally, there have been at least two commercial attempts to develop ultrasound agents for myocardial perfusion imaging [33].

We offer the first agent that utilizes the electrical activity of the heart.

As a result, ours is the first agent that activates selectively in the myocardium for a given set of ultrasound parameters, leaving the ventricle relatively dark while brightening the myocardium. We are optimistic that our approach has the potential to rival single photon emission computed tomography (SPECT) and positron emission tomography (PET) at lower cost and lower risk without a loss in sensitivity or specificity. We recognize that “the history of contrast echocardiography has been characterized by cycles of enormous expectations and subsequent disappointment,” [33,34] yet do not believe that success necessarily “… starts with the microbubble itself, which must be predictably destroyed by high mechanical index (MI) ultrasound but provide stable, high signal-to-noise ratio across a wide range of lower intensity imaging.” [33] We contend that a single MI suffices and that what is needed is an agent that takes advantage of the heart’s electrical activity to allow selective activation.

The voltage-activated phase-change agent described herein satisfies that need.

2. Theory

There are two key points to bear in mind at the outset. First, the electrical fields employed in this work are orders of magnitude lower – even after accounting for particle size – than those associated with electroporation [35–41], and the applied electric field (alternating current, ac) frequency employed in this work is at least an order of magnitude slower than frequencies utilized for ac electroporation [36,42,43]. Second, the (zeta) potentials reported herein are not transmembrane potentials.

Voltage activation begins with making the nesting shell charged to interact with the electrical activity of the heart. The surface potential of the nesting shell depends on the surface charge density, and the weakening of this potential with distance away from the nesting shell depends on the ionic strength of the solution and the radius of the nest. In the case of a bilayer, it is possible for both the inner and outer leaflets to be charged and for the ionic strength to be different in the different aqueous compartments that exist inside and outside the bilayer. The situation is similar to that of spontaneous vesicles comprising mixtures of cationic and anionic surfactants [44].

When a charged entity (e.g., an ion, a charged nest, or a charged molecule or charged domain within a nesting shell) experiences an electric field, E, that entity can move (e.g., translation or rotation) or deform, or both. In the case of translation, the entity accelerates until the viscous drag force matches the force that caused the acceleration. What is relevant for the current work is that the force due to electric field depends on charge, whereas the drag force depends on size. Accordingly, the various charged entities in the system can therefore experience different accelerations, depending on the charge-to-size ratio, and this can lead to structural shifts.

The entity eventually reaches a terminal velocity, v, that is proportional to the electric field as described by Eq. (1).

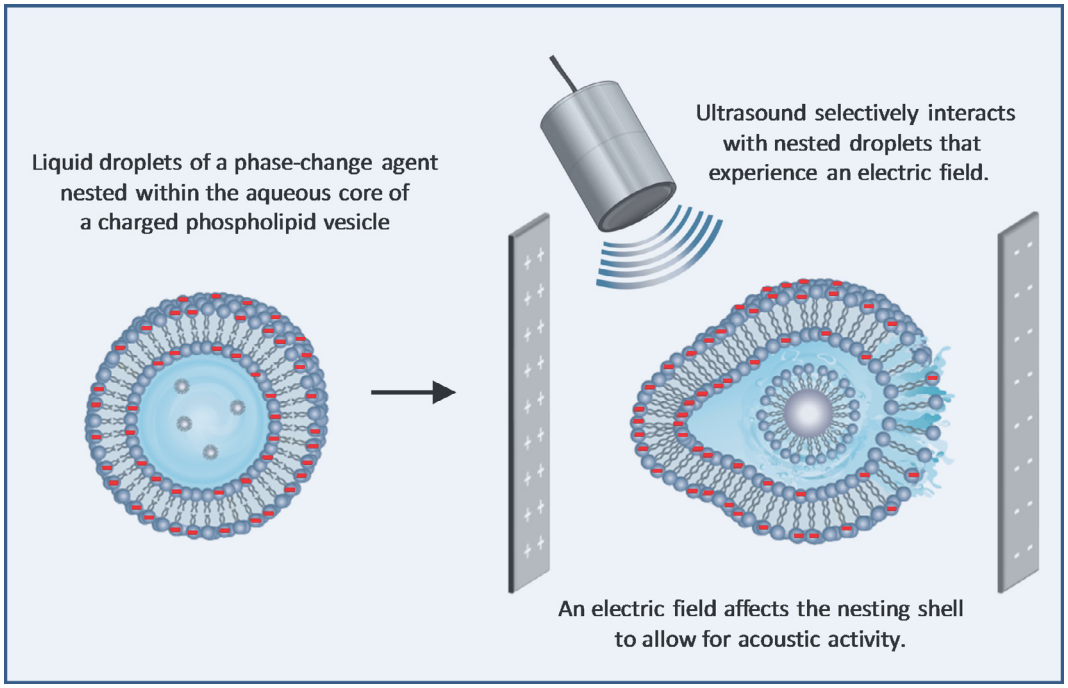

Fig. 1. Nested PCA emulsion and voltage activation: Illustration of a nested emulsion construct, in which coated droplets of a phase change agent (e.g., a perfluorocarbon) reside within the aqueous interior of a vesicle (or microcapsule). The nesting shell illustrated here depicts phospholipids, though other nesting shell materials could be used. In the case of phospholipid bilayer nesting shells, the formulation might include additional species (e.g., cholesterol or triglycerides, or both). Moreover, multiple phospholipid species that differ in chain length and saturation and head group type, size, and charge (cationic, anionic, zwitterionic, or non-ionic) could be used, and structures other than the ones depicted here can arise from the formulation. The dashes in the illustration indicate negative charges; (positive) counter-ions are not shown, and zeta potentials in this work should be not be confused with transmembrane potentials. The presence of an electric field affects the charged nesting shell to allow for acoustic activity. Note that the electric fields used in this work are orders of magnitude less than those associated with electroporation. The illustration is not to scale and not intended to convey technical details or mechanistic phenomena. *Source:* Jennifer Bing, Director of Program Initiatives, Drexel University, College of Engineering, 2017.

$$v = \frac{QE}{6\pi\eta R} \tag{1}$$

where Q is total charge of the entity, R is radius of the charged entity, and η is the viscosity of the medium. It is worth noting that the values of Q and R in Eq. (1) are not, generally speaking, those associated with the surface of the charged entity. This is because a layer of counter-ions can move with the charged entity, defining a so-called slipping plane or plane of shear; the location of the slipping plane is not known *a priori*, though it resides outside the Stern layer and within the diffuse double layer in the case of a charged particle. Common practice is to treat the charged entity and the layer of carried counter-ions as a unit and to define a zeta potential, ζ, as the electric potential at the slipping plane. [45] Solution of the Poisson-Boltzmann equation for spherical geometry in the Debye-Hückel limit of low potential shows that the zeta potential, like the terminal velocity, depends on the ratio (Q/R). By invoking the definition of electrophoretic mobility, U, which is the terminal velocity divided by the electric field ($U = v/E$), one obtains the Henry equation

$$U = \frac{\epsilon_r \epsilon_o}{\eta}\zeta f(\kappa a) \tag{2}$$

where ε_r is the relative permittivity of the medium, ε_o is the permittivity of a vacuum, κ is the inverse Debye length, and a is the radius of the entity that moves [46]. Appearing in Eq. (2) is Henry's function, f(κa), which ranges from 1 in the Smoluchowski limit of a thin double layer ($\kappa a > 300$) to 2/3 in the Hückel limit of a thick double layer ($\kappa a < 0.5$). [46,47][1] Accordingly, one can tailor sizes and charges to achieve a desired electrophoretic mobility for the nested structure as as a whole. Depending on the charge-to-size ratios used, the acceleration that gives rise to this electrophoretic mobility of the nested structure could be the same or different than the acceleration of the charged entities within the nested structure. Herein we demonstrate the responses of two nesting shell chemistries to electric fields of varying strength.

[1] Some publications report the Henry function as ranging from 1 in the Hückel limit to 1.5 in the Smoluchowski limit, but the function presented in the 1931 paper by Henry [46] is as described herein.

3. Materials and methods

3.1. Materials

Phospholipids, sterols and triglycerides were purchased from Avanti Polar lipids (Alabaster, AL. USA). Perfluorocarbons were purchased from FluoroMed, L.P. (Round Rock, TX, USA). Calcein, cobalt (II) chloride, poly vinyl alcohol (MW = 27,000 & 85,000 – 124,000) and surfactant (polysorbate 20) were purchased from Sigma Aldrich (St. Louis, MO). All chemical species were used without further purification.

3.2. Methods

3.2.1. PCA nanoemulsion

A perfluorocarbon nanoemulsion comprising perfluoropentane, surfactants and water, was prepared via probe sonication (Model UP200S Hielscher – Ultrasound Technology, Teltow, Germany) at 20 kHz and 50% amplitude. A typical batch yielded an average diameter of approximately 350 nm, measured by dynamic light scattering (NanoBrook Omni, Brookhaven Instruments Corp., Holtsville, NY). An average diameter of approximately 255 nm was obtained when nanoemulsions were made with perfluorobutane via microbubble condensation. The amounts of perfluorocarbon and surfactant used to prepare the nanoemulsions were 5.00% v/v and 0.08% v/v, respectively.

3.2.2. Nesting the PCA nanoemulsion

Nesting proceeds via double emulsion, as described previously.[16] Different membrane components were used here to give desired nesting shell properties, and, strictly speaking, nesting of PCAs constitutes a triple emulsion (oil in water in oil in water, or O/W/O/W). A typical batch involved diluting 500 μL of the first emulsion (that is, the PCA nanoemulsion, O/W) with 500 μL of PBS (or, in the case of fluorescence leakage experiments, 1 mM calcein) and adding this first emulsion to 1 mL of a lipid mixture in chloroform and homogenizing using a Polytron PT3100 (Kinematica Inc., Lucerne, Switzerland) for 1 min at 12,000 RPM to give a double emulsion (O/W/O). The double emulsion was then added to 8 mL of 2% PVA (27,000 MW) in water to give a triple emulsion (O/W/O/W), which was homogenized for 2 min (again at 12,000 RPM with the Polytron PT3100). The extant triple emulsion was then added to an additional 8 mL of 2% PVA (27,000 MW) in water and placed on a magnetic stirrer for 24 h.

Two nesting shell formulations were utilized herein: Formulation I comprised 20 mol% 1,2-distearoyl-*sn*-glycero-3-phosphocholine (DSPC), 20 mol% 1-stearoyl-2-oleoyl-*sn*-glycero-3-phospho-1′-*rac*-glycerol (SOPG), 40 mol% cholesterol, and 20 mol% triolein; and Formulation II comprised 20 mol% 1,2-distearoyl-*sn*-glycero-3-phospho-1′-*rac*-glycerol (DSPG), 20 mol% 1-stearoyl-2-oleoyl-*sn*-glycero-3-phosphocholine (SOPC), 40 mol % cholesterol, and 20 mol% triolein. The size distributions of the two nesting shell chemistries were measured with a Beckman Coulter counter (Multisizer 4E); Formulation I gave total count of 3.00×10^9 particles/mL, a mean size of 1.66 μm, and a median size of 1.42 μm, and Shell II gave a total count of 3.13×10^9 particles/mL, a mean size of 1.67 μm, and a median size of 1.44 μm.

3.2.3. Fluorescence leakage experiments

3.2.3.1. Home-built (3-D printed) housing for fluorescence spectrometer. To measure ultrasound-induced or electric field-induced, or both, fluorescence leakage in real time, a custom housing was designed using CREO Panametrics 3.0 software (PTC, Boston, MA) and 3-D printed on a Dimension Elite 3D Printer (Stratasys, Eden Prairie, MN). The home-built housing was printed in Drexel University's Machine Shop with 1.78 mm thick ABS filament (ABS P430™ Model (Ivory)) and with a solid internal structure and subsequently exposed to acetone vapor for 1 h to make the system water-tight. Fig. 2 depicts the housing, which screws into the base of a steady-state fluorimeter (A-710, Photon Technology International Inc., Birmingham, NJ) in place of an existing cuvette holder. The basin that sits atop the pegs holds deionized water and provides a focal distance of 7.5 cm. The inside of the basin was coated with 3 layers of epoxy (to ensure that deionized water could not escape from the basin). A thin sheet of polyvinyl chloride (PVC) separates the deionized water from the sample; this sheet is acoustically transparent and does not affect the fluorescence intensity of calcein.

3.2.3.2. High-frequency ultrasound. Ultrasound was delivered using a 5 MHz, 7.5 cm focused ultrasound transducer (Olympus NDT, Waltham, MA, USA), driven by an 8116A function generator (Hewlett-Packard, Palo Alto, CA) in series with a +55 dB ENI 3100LA power amplifier (ENI, Rochester, NY). In this study, the transducer was used to deliver a desired peak negative pressures (PNP), which was measured using a calibrated HGL-0200 hydrophone (ONDA Corp., Sunnyvale, CA). The excitation pulse consists of 10 sinusoidal waveforms with a 40 μs pulse repetition time, corresponding to a 5% duty cycle. The ultrasound transducer is submerged into the 3-D printed ultrasound housing shown in Fig. 2 such that its focal volume is within the light path traced by the fluorescence spectrophotometer. A 0.8 cm silicone rubber sheet was placed at the bottom of the quartz cuvette to avoid standing waves.

3.2.3.3. Electric field parameters. Potentials of desired voltage were applied using an Agilent 33220A function generator (Agilent, Santa Clara, CA) with a sinusoidal waveform at an alternating current of 1 Hz to create electric fields of desired strength across the 99.5% titanium electrodes (Alfa Aesar, Ward Hill, MA) in the cuvette (1 cm width) in Fig. 2. Care was taken to minimize electrochemical reactions, and titanium was chosen as the electrode material as it is inert and highly resistive to common electrochemical reactions at low potentials [48]. Cyclic voltammetry showed that electrochemical reactions were minimal over the voltage window of interest, and absorbance spectra confirmed that electrochemical reactions were not appreciable. Moreover, control studies with calcein and cobalt chloride in the absence of PCA and nesting shell materials ruled out electrochemical reactions as a cause for the observed changes in fluorescence intensities. A hole was punched through the electrode facing the emission monochromator to allow for transmission of light from the sample to the detector.

3.2.3.4. Calcein assay. Calcein leakage was measured via standard protocol [16]. Suspensions of nested PCAs were diluted by a factor of 20× in a cobalt chloride solution. Dilution was necessary to reduce the optical density to a value less than 0.2 so as to prevent the attenuation of fluorescence intensities that would otherwise arise from light scattering via the well-known inner filter effect. The dilution was performed with cobalt chloride, the concentration of which matched calcein nearly 1:1 on a molar basis, for two reasons: first, it minimized osmotic stress owing to variations in ionic strength across the liposomal bilayer, which could cause leakage and complicate the analysis; and second, it quenched external calcein. Samples were pipetted into quartz cuvettes, which were placed into the 3-D printed housing described above. Samples were exposed to varying (high-frequency ultrasound) insonation pressures, electric potentials, and combinations of the two, and fluorescence intensities recorded during exposure to the varying acoustic and electric field modalities. A sample that was not exposed to high-frequency ultrasound or electric field served as a control.

Calcein leakage was measured over 40-min intervals using the A-710 steady-state fluorescence spectrometer (Photon Technology International Inc., Birmingham, NJ) with 2-nm slit widths, 1.0-s integration time, and 1-nm step size. Emission spectra (490–540 nm) were obtained using a 475-nm excitation wavelength. Calcein leakage (% of maximal) was calculated by Eq. (3), where F_t is the fluorescence intensity of the sample at time t, F_0 is the initial fluorescence intensity (which defines 0% release), and F_{100} is the fluorescence intensity at the conclusion of the experiment after probe sonication at high intensity and low frequency (20 kHz) (which defines 100% release). The leakage values reported herein do not capture any passive (meaning the absence of applied fields) leakage that might occur prior to the measurement of F_0, which means that the assay could potentially under-report the amounts of leakage that actually occurred. Passive leakage does not appear to be significant, however, based on observations of control samples. Specifically, the value of F_0, which was measured immediately (meaning within tens of seconds) after sample preparation, was not sensitive to time; control samples showed little-to-no change in fluorescence intensity for the duration of the experiment, suggesting that passive leakage, if it did occur, was complete prior to the measurement of F_0. If that were the case, though, then one would expect no additional leakage upon exposure to high-intensity, low frequency (20 kHz) sonication, yet the same control samples that exhibited little-to-no change in fluorescence intensity for the duration of the experiment then showed an approximately fourfold change in fluorescence intensity when sonicated. Taken together, these observations point to a lack of appreciable leakage in the absence of applied fields.

$$\%\ Leakage = \frac{F_t - F_0}{F_{100} - F_0} * 100 \tag{3}$$

Data is presented as an average of runs with error bars denoting standard deviations. Absorbance was measured with a Lambda 40 UV–VIS spectrometer (Perkin Elmer, Waltham, MA) to confirm that electrochemical reactions were not appreciable.

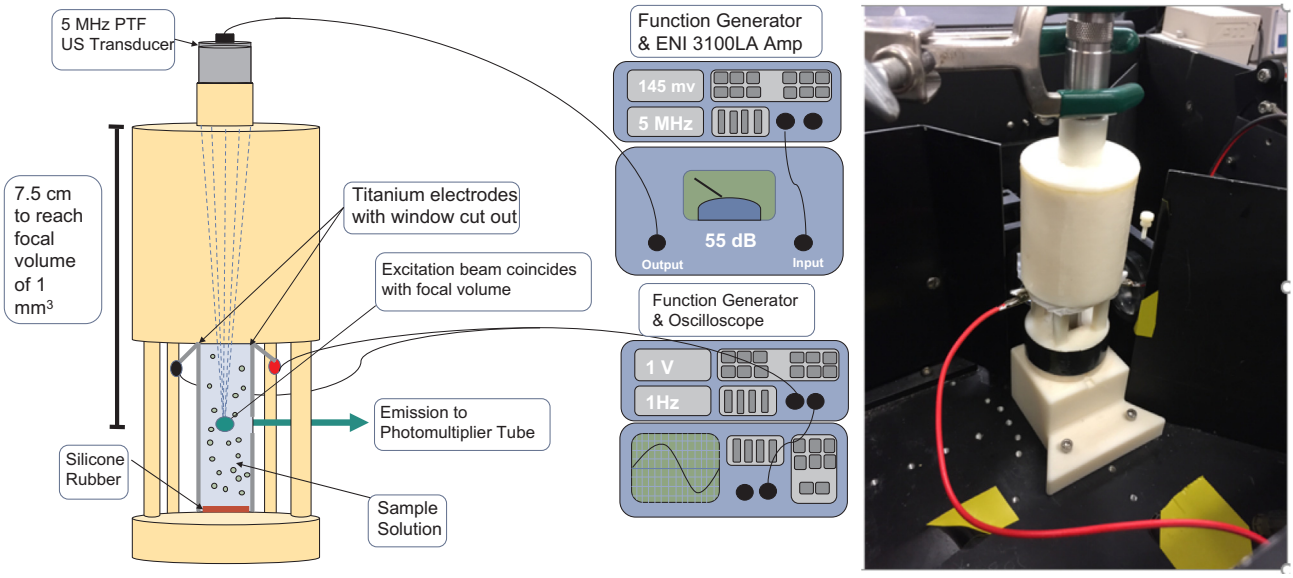

Fig. 2. Custom, 3-D printed housing for live fluorescence measurements in presence of ultrasound or electric field, or both: (Left): Illustration of the fluorescence assay experimental set-up. The ultrasound transducer is placed into the top of the 3-D printed basin with its focal distance of 7.5 cm located within the cuvette at the height where the excitation light beam passes through the sample. Titanium electrodes are positioned 1 cm apart, and alligator clips are used to create varying sinusoidal potentials using a function generator; the electrode facing the emission monochromator has a hole to allow for passage of light to the detector. (Right): Photograph of the custom, 3-D printed housing inside the A-710 steady-state fluorescence spectrometer (Photon Technology International Inc., Birmingham, NJ).

3.2.4. Electrophoretic mobility

Electrophoretic mobilities were measured on a Brookhaven NanoBrook Omni (Brookhaven Instruments Corp., Holtsville, NY), which employs phase Analysis Light Scattering (PALS). The system uses a 35 mW red diode laser with a nominal wavelength of 640 nm with an effective scattering angle of 15°. Samples were diluted with DI water, and electrophoretic mobility was measured at a fixed potential of 4 V alternating at 2 Hz. Zeta potential was calculated via Eq. (2) in the Smoluchowski limit.

3.2.5. Tissue phantom experiment

3.2.5.1. Tissue phantom preparation. A poly(vinyl alcohol) (PVA) cryogel phantom composed of 10 wt% PVA (85,000–124,000 MW) is used as a tissue mimicking phantom, as described by Surry et al. [49]. Briefly, a 1.5 L solution of 10 wt% PVA is heated to 80 °C for 12 h to allow for the polymer to solubilize. The beaker is covered with aluminum foil during the heating process to minimize water loss due to evaporation. Once the solution is fully dissolved, it is poured into a stainless-steel phantom mold that has a cylindrical sample chamber as shown in Fig. 3A and is left at room temperature for 24 h to allow air bubbles to escape.[16] The solution then undergoes three freeze–thaw cycles so that the PVA aligns into a tight crystal structure.[3] The speed of sound and tissue density increase with the freeze–thaw cycles; after three cycles the acoustic properties closely match human tissue, with the speed of sound in the phantom measured at 1535 m/s and the attenuation coefficients ranging from 0.075 to 0.28 dB (cm MHz)$^{-1}$ [49]. The PVA cryogel is kept at 4 °C in deionized water to avoid dehydration of the gel. A razor blade was used to cut out slices that are 5 cm in length and 8 cm in depth to allow for aluminum electrodes to be placed 6 cm apart as shown in Fig. 3A. This tissue-mimicking phantom allows for brightness studies in which intensities within the sample region are compared to intensities within the PVA tissue-mimicking region for different combinations of ultrasound and electric field parameters.

3.2.5.2. Contrast-to-tissue ratio (CTR). Brightness (B) mode images were taken from a GE Vivid *i* (GE Medical Systems Information Technologies GmbH, Freiburg, Germany) portable clinical ultrasound machine to evaluate the contrast-to-tissue ratio (CTR) for different formulations subjected to a fixed ultrasound intensity with various electric fields. The GE Vivid *i* was set to 0.28 MI in the harmonic imaging mode with frequencies of 2.0 and 4.0 MHz (transmit and receive, respectively) with the use of a 2 MHz wide-band phased array transducer (GE 3S-RS) while the electric field between the electrodes was varied from 0 V/cm to 3 V/cm. The volume of the sample chamber within the PVA cryogel was 40 mL; in a typical experiment, 2 mL of a given formulation were added into 38 mL DI water. The phased array transducer was placed horizontally against the front face of the PVA cryogel with coupling gel, and the phantom was placed on a magnetic stir plate to allow mixing of the sample contents during experiments.

Fig. 3B shows the type of image obtained during the study and denotes two regions, the sample contrast region and the tissue-mimicking region. These regions remain the same for the entirety of the experiment. Contrast-to-tissue ratios were calculated from obtained images using a MATLAB program that digitized the recorded images, converting them to grayscale intensities ranging from 0 (black) to 255 (white). The brightness of the pixels was averaged, and the CTR value was calculated from individual brightness values via Eq. (4), where I_C and I_T are the grayscale intensities of the contrast and tissue regions, respectively, as calculated by the MATLAB program [4].

$$\textit{Contrast to Tissue Ratio} = 20\log_{10}\left(\frac{I_C}{I_T}\right) \tag{4}$$

3.2.6. Animal studies

All animal experiments complied with legal requirements and guidelines set by Drexel University's Institutional Animal Care and Use Committee (IACUC).

3.2.6.1. Small animal. Studies were done with Sprague-Dawley rats under general anesthesia. A high-frequency, high-resolution digital imaging platform with linear array technology and Color Doppler Mode for *in vivo* high-resolution micro-imaging was used for (closed chest) echocardiography (Vevo® 2100 Imaging System, FUJIFILM VisualSonics Inc., Toronto, Canada). To provide appropriate resolution and depth of penetration necessary, a high-frequency transducer probe (VisualSonics MS400 with a frequency range of

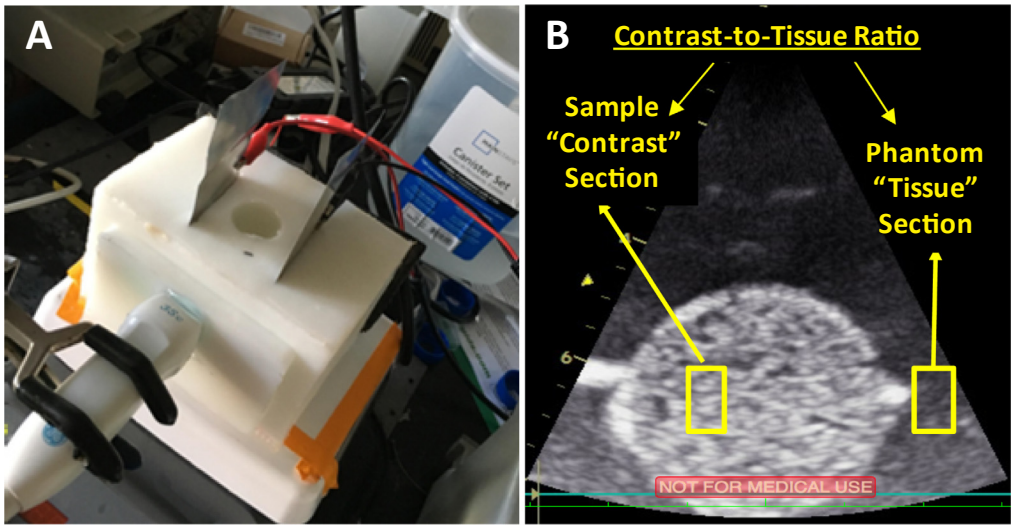

Fig. 3. Tissue-mimicking phantom: (A) photograph showing the ultrasound transducer of GE Vivid *i* in contact with the PVA cryogel tissue phantom. The two aluminum plates are inserted into the phantom 6 cm apart and span the sample region that has a diameter of 3 cm. (B) screenshot of an image generated using the GE Vivid *i*, showing the contrast-to-tissue ratio (CTR) methodology. Both regions chosen for brightness analysis are approximately 6 cm away from where the transducer couples to the phantom. The sample "contrast" (C of CTR) section is shown within the 3-cm circular sample cavity, while the "tissue" (T of CTR) section is outside the sample cavity.

18–38 MHz; operated at 21 MHz and 5% power) was utilized for the assessment of cardiovascular function and enhancement of the myocardium. In addition to the VisualSonics transducer used for imaging, the 2 MHz wide-band phased array transducer (GE 3S-RS; that is, the very same transducer that was used with the GE Vivid *i* in the tissue-mimicking phantom studies) was used for excitation (0.07–0.28 MI).

3.2.6.2. Large animal. Studies were done with swine under general anesthesia. Imaging (closed chest) and excitation were performed with the same GE Vivid *i* and probe that were used for the tissue-mimicking phantom studies.

4. Results

4.1. In vitro studies

4.1.1. Fluorescence leakage studies

Fig. 4 shows calcein leakage from a formulation of nested PCA under three conditions: an electric field of 0.25 V/cm applied alone; ultrasound of 0.5 MPa PNP applied alone; and an electric field of 0.25 V/cm plus ultrasound of 0.5 MPa PNP applied simultaneously. Each modality alone produces measurable leakage, and the two modalities, when used in combination, exhibit a synergistic effect. This is evident if one compares the result of the combined modalities with what would be expected by simply adding the results of the individual modalities, the latter of which is depicted in Fig. 4 as a thin grey line devoid of symbols.[46]

4.1.2. CTR (Brightness) studies in a Tissue-Mimicking phantom

Fig. 5 shows how ultrasound imaging brightness responds to an electric field for two nesting shell formulations. The first nesting shell, which gave a zeta potential of ~ −60 mV, showed some visual evidence of brightening upon application of an electric field of 1.0 V/cm but did not exhibit clearly discernible (to the eye) additional brightening upon increasing the electric field strength to 3.0 V/cm. The second nesting shell, which gave a zeta potential of ~ −70 mV, showed ample visual evidence of brightening, both upon application of an electric field of 1.0 V/cm and upon increasing the electric field strength to 3.0 V/cm. The qualitative visual brightness results were quantified using the CTR methodology and are given in Fig. 6, which also shows how the voltage difference between the two metal plates in the tissue-mimicking phantom was varied throughout the experiment.

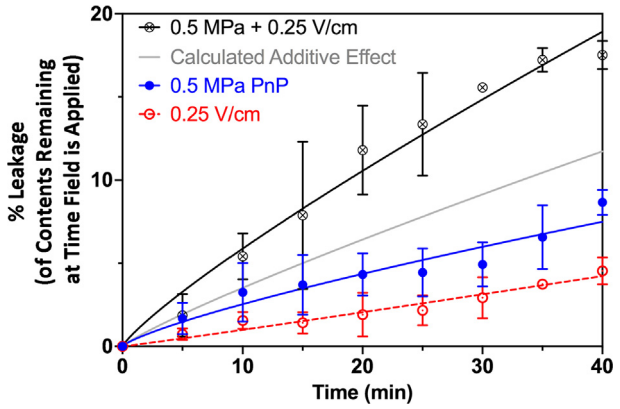

Fig. 4. Synergistic Calcein release caused by ultrasound plus electric field: Temporal calcein leakage is shown for samples that were exposed to an electric field of 0.25 V/cm alone (open circles), ultrasound of 0.5 MPa PNP alone (solid circles), and both an electric field of 0.25 V/cm and ultrasound of 0.5 MPa PNP (circles filled by x's). The thin line devoid of symbols shows the "Calculated Additive Effect," which is the leakage profile obtained by adding the results of the individual modalities. The fact that the combined modalities give rise to a leakage profile that is above the "Calculated Additive Effect" indicates a synergy between ultrasound and electric field. Lines are drawn through data points to aid the eye.

4.2. In vivo studies

4.2.1. Rat studies

Fig. 7 shows B-mode images of a rat heart (closed chest) during diastole. Panel A shows a baseline image obtained prior to administration of any agent. Panel B is an image obtained after administering a nested formulation with nesting shell chemistry II, which gave superior brightness in the tissue phantom studies. Panel C is an image obtained after administering a nested formulation with nesting shell chemistry I, and panel D is an image obtained after administering un-nested microbubbles of sulfur hexafluoride coated with a saturated phospholipid. Whereas traditional, un-nested microbubbles brighten the ventricle but not the myocardium (compare panel D with panel A), the nested PCA formulations do the converse (e.g., compare panel B with panel A), and the level of contrast enhancement observed depends on the nesting shell formulation used (compare panel C with panel B).

4.2.2. Swine studies

Fig. 8 shows B-mode images of a pig heart (closed chest, long axis view) obtained with a GE Vivid *i* (the very same unit used for the tissue-

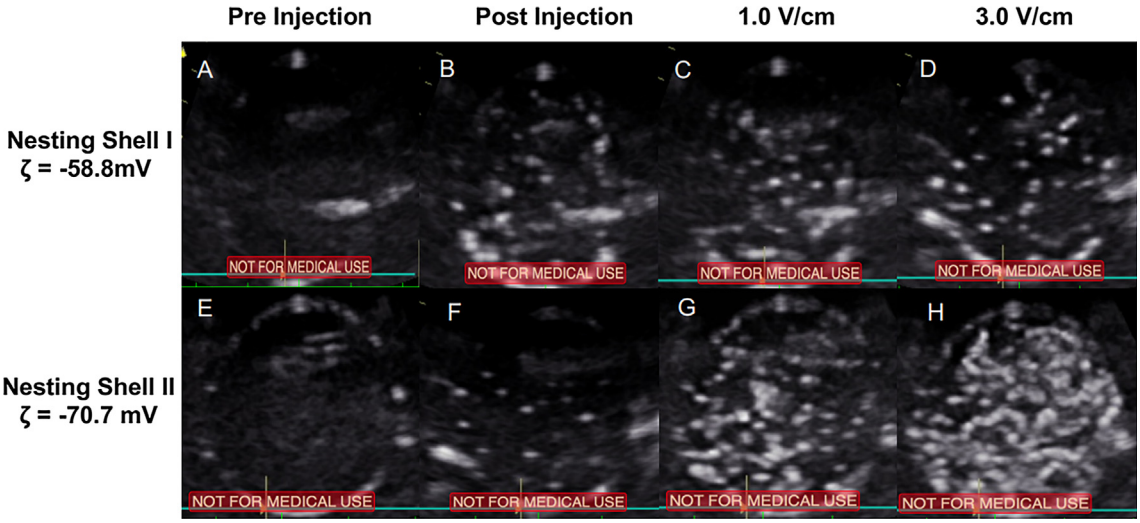

Fig. 5. Voltage-activated ultrasound brightness in a tissue-mimicking phantom: The influence of an electric field on ultrasound imaging (GE Vivid *i*, 0.28 MI, 2.0/4.0 MHz) brightness is shown for nesting shell chemistries I and II, which resulted in zeta potentials of ~ −60 mV (top row) and ~ −70 mV (bottom row), respectively. Panels A and E are images taken before the samples were added, at which point the sample chamber contained just DI water, in the absence of an electric field. Panels B and F are images taken immediately after 2 mL of sample were added to the phantom and before application of an electric field. Panels C and G are images taken when the electric field was 1.0 V/cm; image G exhibits enhanced brightness when compared with image F, whereas brightening in panel C relative to panel B is more difficult to discern. Panels D and H are images taken when the electric field was 3.0 V/cm; image H exhibits enhanced brightness relative to image G, whereas brightening in panel D relative to panel C is not evident. These qualitative brightness results are quantified via the CTR methodology and shown in Fig. 6.

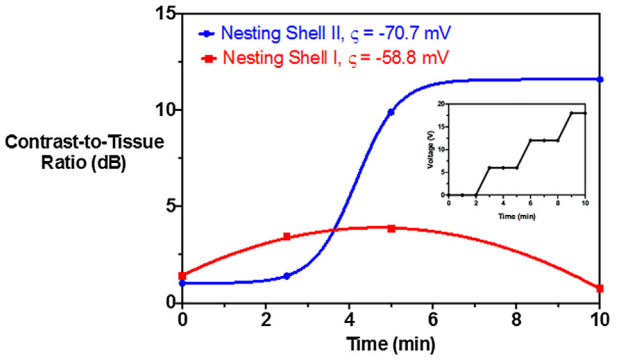

Fig. 6. Voltage-activated ultrasound brightness in a tissue-mimicking phantom quantified by CTR: The results of Fig. 5 were quantified using the CTR methodology and presented as CTR versus time. The inset graph shows how the voltage difference between the two metal plates in the tissue-mimicking phantom was varied throughout the experiment.

mimicking phantom studies) at baseline and after administering the nested formulation with nesting shell chemistry II, which gave superior results in both the tissue-mimicking phantom and rat heart imaging studies. As was the case for the *in vitro* and rat studies, the nested PCA formulation showed selective activation within the swine myocardium.

5. Discussion

The ability of applied and endogenous electric fields to influence cellular physiology is well known, as is the amplification of the electric field that arises by establishment of a transmembrane potential (across what is a thin cell membrane) [50]. Indeed, the influence of an electric field on the cell often correlates with the magnitude of the transmembrane potential, which depends not only the strength of the electric field but also - among other factors - on the radius of the object (e.g., a cell or a liposome) that the membrane envelops [38,50]. One well-known impact of an electric field on a cell membrane or vesicle bilayer is electroporation [51], which occurs when the transmembrane potential is sufficiently large to achieve dielectric breakdown and enable current flow (and other molecular transport) across pores that interrupt

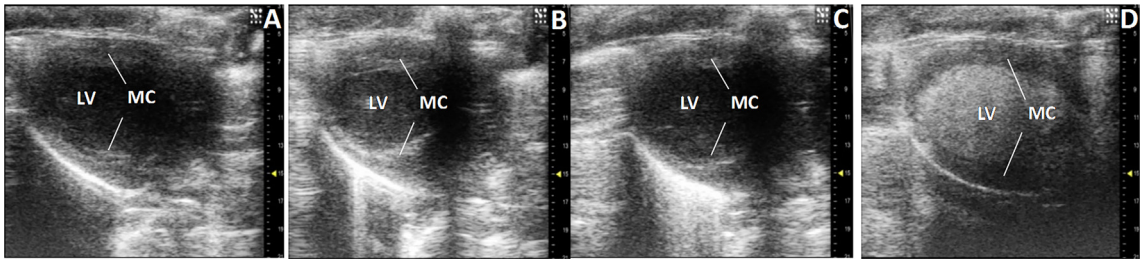

Fig. 7. Voltage-activated ultrasound contrast in rat heart: B-mode images of a rat heart (closed chest) during diastole are shown for the following conditions: (A) at baseline prior to administration of any agent; (B) after administering a nested formulation with shell chemistry II; (C) after administering a nested formulation with shell chemistry I; and (D) after administering un-nested microbubbles of sulfur hexafluoride coated with a saturated phospholipid. LV denotes Left Ventricle, and MC denotes MyoCardium. Nesting shell chemistry II shows brightening of the myocardium relative to baseline, and shows some evidence of activation within the left ventricle (compare panels B and A). However, the brightening of the ventricle is far less, and the brightening of the myocardium far greater, than what is obtained with un-nested microbubbles (compare panels B and D). Nesting shell chemistry I gave a result similar to that of nesting shell chemistry II, though the effect was less pronounced (compare panels B and C).

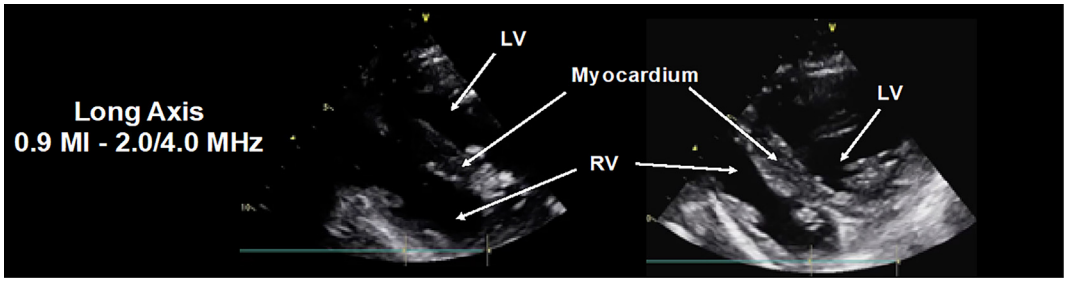

Fig. 8. Voltage-activated ultrasound contrast in Swine Myocardium: Long-axis view of a swine heart (closed chest) showing pre- (left image) and 30 s post-injection (right image) of nesting chemistry II. LV denotes left ventricle, and RV denotes right ventricle. The contrast enhancement between the myocardium and the left ventricle increases by 36.4 dB ± 0.2 upon injection of the voltage-activated, nested PCA formulation.

the membrane [39,41]. The upshot in the context of the current work is that electroporation is not expected to occur, given the electric field strengths and nest diameters used herein; this means that voltage activation likely proceeds via a different mechanism or mechanisms. We note that electric fields can produce intramembrane effects [50,52].

Although one can imagine applications involving *applied* external fields, for which one can control the electric field strength to achieve a desired effect, this paper addresses an application, namely myocardial perfusion imaging, that involves an *endogenous* electric field. In lieu of controlling the electric field, we take advantage of the electric field the heart produces, which varies in time and space [53–57].

The results of rat and swine studies demonstrate the feasibility and clinical relevance of such an approach, showing selective enhanced ultrasound contrast in the myocardium – where the electric field is stronger than in other regions showing less enhancement. The swine study gave the most pronounced selective contrast enhancement, as the rat study showed some activation within the left ventricle. This result might be explained in part by differences in attenuation, relating in part to differences in penetration depths (skin to organ), between the animals.

The *in vitro* studies confirm the results of the animal studies and demonstrate that voltage-sensitivity is tunable with chemistry. In particular, nesting shell formulation II exhibited a greater propensity to activate and a greater sensitivity to a change in electric field strength than nesting shell formulation I. While the two formulations had different zeta potentials, the difference in nesting shell chemistry was not merely a difference in the fraction of charged species. Thus, the type, size, valence, and location, in addition to amount, of charged species can influence the response to an electric field. Although the two shell chemistries yielded similar size distributions, it is also possible that some of the variation observed in the two formulations might be attributable to variations in numbers of droplets or bubbles or volumes of gas, which are known to influence echogenicity.[58]

6. Conclusions

Evidence from *in vivo* studies shows the feasibility of selective activation of a voltage-sensitive ultrasound contrast agent at a fixed MI. Leakage studies *in vitro* and brightness studies in a tissue-mimicking phantom support the *in vivo* findings and demonstrate that the system is somewhat tunable. Examples of parameters that influence the sensitivity of the nested PCA architecture to an electric field are nest curvature and charge, including type of charge, size of charged entity, amount of charge, and location of charge. Chemical composition of uncharged species also plays a role. The sensitivity to voltage enables activation of a sub-set of nested liquid perfluorocarbon droplets, namely those in the presence of an electric field, at a fixed ultrasound intensity. Reaction of the nesting shell to an electric field facilitates activation at the prevailing MI, which is otherwise insufficient to produce detectable acoustic activity. Although an electroporation reaction is unlikely, given the magnitudes of the electric fields involved, some other remodeling of the bilayer due to the presence of an electric field is possible and perhaps probable. Selective activation utilizing an electric field, regardless of mechanism, makes this voltage-sensitive phase change agent well-suited for myocardial perfusion imaging. Time will tell how well.

Acknowledgments

We recognize and thank Dr. Richard Huneke, DVM, MPH and Emily Reimold MLAS, LATG from Drexel University Laboratory Animal Resources (ULAR) for their expert clinical and technical support in the handling, management, and care of all the animals studied. Their time, consultation, dedication, skill and professionalism have been an invaluable addition to the advancement of this science from bench to *in-vivo* modeling; indeed, these studies would not have happened without such assistance. This work was supported by the Coulter-Drexel Translational Research Partnership Program; MC was supported in part by the Department of Education (Award Number P200A150240).

References

[1] Wrenn S, et al. Controlling cavitation for controlled release. IEEE Int Ultrason Symp Proc 2009:104–7.
[2] Dicker S, et al. Coencapsulation of lipid microbubbles within polymer microcapsules for contrast applications. Bubble Sci Eng Technol 2011;3(1):12–9.
[3] Wallace N, et al. Influence of nesting shell size on brightness longevity and resistance to ultrasound-induced dissolution during enhanced B-mode contrast imaging. Ultrasonics 2014;54:2099–108.
[4] Bartolomeo A, et al. Nesting microbubbles: influence on acoustic activity and image brightness. Bubble Sci Eng Technol 2012;4(2):78–84.
[5] Wrenn S, et al. MICROCAPSULES: reverse sonoporation and long-lasting, safe contrast. Acoust Imag 2012;31:81–90.
[6] Dierkes J, et al. Quantification of cell death due to ultrasound therapy with both traditional and nested microbubbles. Bubble Sci Eng Technol 2012;4(2):72–7.
[7] Epstein P, Plesset M. On the stability of gas bubbles in Liquid-Gas solutions. J Chem Phys 1950;18(11):1505–9.
[8] Duncan PB, Needham D. Test of the Epstein – Plesset Model for gas microparticle dissolution in aqueous media: effect of surface tension and gas undersaturation in solution. Langmuir 2004;20(7):2567–78.
[9] Borden MA, Longo ML. Dissolution behavior of lipid monolayer-coated, air-filled microbubbles: effect of lipid hydrophobic chain length. Langmuir 2002;18(24):9225–33.
[10] Barletta G, Riccarda Del Bene M. Myocardial perfusion echocardiography and coronary microvascular dysfunction. World J Cardiogr 2015;7(12):861–74.
[11] Porter T, Xie F. Myocardial perfusion imaging with contrast ultrasound. JACC: Cardiovasc Imag 2010;3(2):176–87.
[12] Dicker S, et al. Influence of shell composition on the resonance frequency of microbubble contrast agents. Ultras Med Biol 2013;1828:1192–7.
[13] Wrenn S, et al. Bursting bubbles and bilayers. Theranostics 2012;2(12):1140–59.
[14] Wallace N, et al. Inertial cavitation threshold of nested microbubbles. Ultrasonics 2015;58:67–74.
[15] Nguyen A, Wrenn S. Acoustically active liposome-nanobubble complexes for enhanced ultrasonic imaging and ultrasound-triggered drug delivery. WIRES Nanomed Nanobiotechnol 2014;6:316–25.
[16] Wallace N, Wrenn S. Ultrasound triggered drug delivery with liposomal nested microbubbles. Ultrasonics 2015;63:31–8.
[17] Brown A, Wrenn S. Nanoscale phase separation in DSPC-cholesterol systems. Langmuir 2013;29:9832–40.
[18] Brown AC, Towles KB, Wrenn SP. Measuring raft size as a function of membrane composition in PC-based systems: Part II–ternary systems. Langmuir

2007;23(22):11188–96.
[19] Brown AC, Towles KB, Wrenn SP. Measuring raft size as a function of membrane composition in PC-based systems: Part 1–binary systems. Langmuir 2007;23(22):11180–7.
[20] Small E, Dan N, Wrenn S. Low-frequency ultrasound-induced transport across non-raft- forming ternary lipid bilayers. Langmuir 2012;28:14364–72.
[21] Small E, et al. Ultrasound-induced transport across lipid bilayers: Influence of phase behavior. Colloids Surf A Physiochem Eng Aspects 2011;390:40–7.
[22] Couture O, et al. Investigating perfluorohexane particles with high-frequency ultrasound. Ultras Med Biol 2006;32(1):73–82.
[23] Reznik N, Williams R, Burns P. Investigation of vaporized submicron perfluorocarbon droplets as an ultrasound contrast agent. Ultras Med Biol 2011;37(8):1271–9.
[24] Matsunaga T, et al. Phase-change nanoparticles using highly volatile perfluorocarbons: toward a platform for extravascular ultrasound imaging. Theranostics 2012;2(12):1185–98.
[25] Lin C, Pitt W. Acoustic droplet vaporization in biology and medicine. Biomed Res Int 2013: 13 pages. http://dx.doi.org/10.1155/2013/404361.
[26] Sheeran P, et al. Decafluorobutane as a phase-change contrast agent for low-energy extravascular ultrasonic imaging. Ultras Med Biol 2011;37(9):1518–30.
[27] Sheeran P, et al. Formulation and acoustic studies of a new phase-shift agent for diagnostic and therapeutic ultrasound. Langmuir 2011;27:10412–20.
[28] Mountford P, Borden M. On the thermodynamics and kinetics of superheated fluorocarbon phase-change agents. Adv Colloid Interface Sci 2016;237:15–27.
[29] Lindner J. Phase-conversion nanoparticle contrast agents: do good things come in small packages? Circ Cardiovasc Imag 2016;9(1):4 pages. http://dx.doi.org/10.1161/CIRCIMAGING.115.004374.
[30] Feingold, S., et al., Quantitative volumetric perfusion mapping of the microvasculature using contrast ultrasound. Invest Radiol, 2010;45(10):14 pages. http://dx.doi.org/10.1097/RLI.0b013e3181ef0a78.
[31] Porter T, et al. Targeted transthoracic acoustic acivation of systemically adminstered nandroplets to detect myocardial perfusion abnormalities. Circ Cardiovasc Imag 2016:9(1): 20 pages. http://dx.doi.org/10.1161/CIRCIMAGING.115.003770.
[32] Sontum P, et al. Acoustic Cluster Therapy (ACT) – A novel concept for ultrasound mediated, targeted drug delivery. Int J Pharmac 2015;495:1019–27.
[33] Thomas J. Myocardial contrast echocardiography perfusion imaging: still waiting after all these years. J Am College Cardiol 2013;62(15):1362–4.
[34] DeMaria A, Cotter B, Ohmori K. Myocardial contrast echocardiography: too much, too soon? J Am Coll Cardiol 1998;32(5):1270–1.
[35] Weaver J, Chizmadzhev Y. Theory of electroporation: a review. Bioelect Bioenerget 1996;41:135–60.
[36] Portet T, et al. Destabilizing giant vesicles with electric fields: an overview of current applications. J Membr Biol 2012;245:555–64.
[37] Mostafa E, Tsong Y. Ion selectivity of temperature-induced and electric field induced pores in dipalmitoylphosphatidylcholine vesicles. Biochemistry 1985;24:2884–8.
[38] Teissie J, Tsong Y. Electric field induced transient pores in phospholipid bilayer vesicles. Biochemistry 1981;20:1548–54.
[39] Chang D, Gao P, Maxwell B. High efficiency gene transfection by electroporation using a radio-frequency electric field. Biochimica et Biophysica Acta 1991;1992:153–60.
[40] Kotnik T, et al. Cell membrane electroporation – Part 1: The phenomenon. IEEE Insul Mag 2012(14–23).
[41] Riske K, Dimova R. Electro-deformation and poration of giant vesicles viewed with high temporal resolution. Biophys J 2005;88:1143–55.
[42] Zhan Y, et al. Low-frequency ac electroporation shows strong frequency dependence and yields comparable transfection results to dc electroporation. J Control Release 2012;160:570–6.
[43] Peterlin P. Frequeny-dependent electrodeformation of giant phospholipid vesicles in AC field. J Biol Phys 2010;36:339–54.
[44] Brasher L, Herrington K, Kaler E. Electrostatic effects on the phase behavior of aqueous cetyltrimethylammonium bromide and sodium octyl sulfate mixtures with added sodium bromide. Langmuir 1995;11:4267–77.
[45] Hunter R. Foundations of colloid science vol. 2. New York: Oxford University Press; 2001.
[46] Henry D. The cataphoresis of suspended particles. Part I. The equation of cataphoresis. Proc R Soc London Ser A 1931;133:106–29.
[47] Ohshima H. A simple expression for Henry's function for the retardation effect in electrophoresis of spherical colloidal particles. J Colloid Interface Sci 1994;168:269–71.
[48] Bewer G, Debrodt H, Herbst H. Titanium for electrochemical processes. J Metals 1982;34(1):37–41.
[49] Surry K, et al. Poly(vinyl alcohol) cryogel phantoms for use in ultrasound and MR imaging. Phys Med Biol 2004;49(24):5529–46.
[50] Lojewska Z, et al. Analysis of the effect of medium and membrane conductance on the amplitude and kinetics of membrane potentials induced by externally applied electric fields. Biophys J 1989;56:121–8.
[51] Tsong T. On electroporation of cell membranes and some related phenomena. Bioelectrochem Bioenerg 1990;24:271–95.
[52] Chanda B, et al. Gating charge displacement in voltage-gated ion channels involves limited transmembrane movement. Nature 2005;436:852–6.
[53] Witkowski F, et al. In vivo estimation of cardiac transmembrane current. Circul Res 1993;72(2):424–39.
[54] Katz A. Physiology of the heart. 4th ed. Philadelphia: Lippincott Williams & Wilkins; 2006.
[55] Pomedli S, Lilly L. Pathophysiology of heart disease: a collaborative project of medical students and faculty. In: Lilly S, editor. The Electrocardiogram. 5th ed. Philadelphia: Wolters Kluwer Health/Lippincott Williams & Wilkins; 2011 [Chapter 4].
[56] Grant A. Cardiac ion channels. Circ Arrythmia Electrophys 2009;2:185–94.
[57] Surawicz B. Chou's electrocardiography in clinical practice. 6th ed. Philadelphia: Saunders Elsevier; 2008.
[58] Gorce J, Arditi M, Schneider M. Influence of bubble size distribution on the echogenicity of ultrasound contrast agents: a study of SonoVue™. Invest Radiol 2000;35(11):661–71.